

## Shallow cumulus cloud fields are optically thicker when they are more clustered

Alinaghi, Pouriya; Janssens, Martin; Choudhury, Goutam; Goren, Tom; Siebesma, A. Pier; Glassmeier, Franziska

**DOI**

[10.1002/qj.4783](https://doi.org/10.1002/qj.4783)

**Publication date**

2024

**Document Version**

Final published version

**Published in**

Quarterly Journal of the Royal Meteorological Society

**Citation (APA)**

Alinaghi, P., Janssens, M., Choudhury, G., Goren, T., Siebesma, A. P., & Glassmeier, F. (2024). Shallow cumulus cloud fields are optically thicker when they are more clustered. *Quarterly Journal of the Royal Meteorological Society*. <https://doi.org/10.1002/qj.4783>

**Important note**

To cite this publication, please use the final published version (if applicable). Please check the document version above.

**Copyright**


Other than for strictly personal use, it is not permitted to download, forward or distribute the text or part of it, without the consent of the author(s) and/or copyright holder(s), unless the work is under an open content license such as Creative Commons.

**Takedown policy**

Please contact us and provide details if you believe this document breaches copyrights. We will remove access to the work immediately and investigate your claim.

## RESEARCH ARTICLE

# Shallow cumulus cloud fields are optically thicker when they are more clustered

Pouriya Alinaghi<sup>1</sup>  | Martin Janssens<sup>1,2</sup> | Goutam Choudhury<sup>3</sup> | Tom Goren<sup>3,4</sup> |  
A. Pier Siebesma<sup>1,5</sup> | Franziska Glassmeier<sup>1</sup>

<sup>1</sup>Department of Geoscience & Remote Sensing, Faculty of Civil Engineering and Geosciences, Delft University of Technology, Delft, the Netherlands

<sup>2</sup>Department of Meteorology & Air Quality, Wageningen University & Research, Wageningen, the Netherlands

<sup>3</sup>Department of Geography and Environment, Bar-Ilan University, Ramat Gan, Israel

<sup>4</sup>Institute for Meteorology, Leipzig Universität, Leipzig, Germany

<sup>5</sup>R & D Weather and Climate Models, Royal Netherlands Meteorological Institute (KNMI), De Bilt, the Netherlands

**Correspondence**

Pouriya Alinaghi, Delft University of Technology, Delft, the Netherlands.  
Email: [p.alinaghi@tudelft.nl](mailto:p.alinaghi@tudelft.nl)

**Abstract**

Shallow trade cumuli over subtropical oceans are a persistent source of uncertainty in climate projections. Mesoscale organization of trade cumulus clouds has been shown to influence their cloud radiative effect (CRE) through cloud cover. We investigate whether organization can explain CRE variability independently of cloud-cover variability. By analyzing satellite observations and high-resolution simulations, we show that more clustered cloud fields feature geometrically thicker clouds with larger domain-averaged liquid water paths, smaller cloud droplets, and consequently larger cloud optical depths. The relationships between these variables are shaped by the mixture of deep cloud cores and shallower interstitial clouds or anvils that characterize cloud organization. Eliminating cloud-cover effects, more clustered clouds reflect up to 20 W/m<sup>2</sup> more instantaneous shortwave radiation back to space.

**KEYWORDS**

cloud microphysics, cloud organization, cloud radiative effect, partial correlation

## 1 | INTRODUCTION

Marine shallow cumulus clouds, as the most prevalent cloud type (Johnson *et al.*, 1999), play a vital role in the climate system by reflecting incoming solar radiation back to space (Bony *et al.*, 2004; Bony *et al.*, 2015; Bony & Dufresne, 2005). Alongside the uncertain response of cloud-controlling factors to climate change, the response of these clouds to changes in cloud-controlling factors is a long-standing uncertainty of model-based climate projections (Nuijens & Siebesma, 2019; Schneider *et al.*, 2017). Recently, observations of contemporary climate have constrained this response (Cesana & Del Genio, 2021;

Myers *et al.*, 2021) but also emphasized the importance of the mesoscales, which climate models do not represent correctly (Vogel *et al.*, 2022).

Shallow cloud fields in the trades exhibit a diverse range of mesoscale patterns (Bony *et al.*, 2020; Stevens *et al.*, 2020). A comprehensive analysis by Janssens *et al.* (2021) shows that the quantification of such patterns needs at least two effective dimensions. Cloud fraction  $f_c$ , as a bulk one-dimensional (1D) measure, and the organization index  $I_{org}$ , which quantifies the level of non-randomness in the cloud spatial distribution within a cloud field (Tompkins & Semie, 2017; Weger *et al.*, 1992), are an example of a suitable variable choice to represent

these two dimensions. How relevant this mesoscale organization is for the low-cloud climate feedback remains an open question.

The shortwave (SW) and longwave (LW) radiative effects of trade cumulus clouds are sensitive to organization (Denby, 2020). The daily mean cloud radiative effect (CRE) varies by approximately  $10 \text{ W/m}^2$ , primarily due to differences in  $f_c$ , with a variability of about  $5 \text{ W/m}^2$  at a fixed  $f_c$  (Bony *et al.*, 2020, Fig. 5). Contrary to the case of deep convective clouds (Tobin *et al.*, 2012), where outgoing LW radiation increases with clustering, Luebke *et al.* (2022) suggest a correlation between increased  $I_{\text{org}}$  values and *reduced* LW warming. No influence of clustering on SW cooling is observed in their study. For stratocumulus cloud decks, McCoy *et al.* (2022) demonstrate that different morphologies, indicative of differences in the horizontal organization of the cloud decks, modulate the relationship between albedo and  $f_c$ .

We aim to investigate whether—independent of  $f_c$  variability—the horizontal organization of shallow cumulus cloud fields has an impact on their net CRE. To do so, we combine satellite data with a large ensemble of large-eddy simulations by Jansson *et al.* (2023) (Section 2). After removing the confounding effect of cloud fraction (Section 3.1), we show that clustered cloud fields feature optically thicker clouds (Section 3.2). This stems from clouds in clustered fields containing more liquid water and smaller retrieved cloud droplets (Section 3.2). In turn, analyzing the simulations establishes that the increases in liquid-water path with clustering result primarily from increases in cloud geometric thickness (Section 3.3). Section 4 concludes.

## 2 | METHODOLOGY AND DATA

To disentangle the effects that spatial organization may have on the CRE independently of  $f_c$ , we adopt the following simple model. Firstly, CRE consists of SW and LW CRE at the top of the atmosphere. In a single cloudy column, SWCRE depends on both  $f_c$  and cloud albedo  $A_c$ , approximately as

$$\text{SWCRE} \approx f_c A_c S_0, \quad (1)$$

where  $S_0$  is the incoming solar radiation (Ramanathan *et al.*, 1989). Three-dimensional radiative effects could alter the SWCRE significantly, yet Singer *et al.* (2021) demonstrated that neglecting these effects has a small effect at the top of the atmosphere for trade cumulus clouds. We therefore relate  $A_c$  to cloud optical depth  $\tau_c$  through the plane-parallel assumption (Lacis & Hansen, 1974):

$$A_c = \frac{\tau_c}{\tau_c + 7.7}. \quad (2)$$

The cloud optical depth  $\tau_c$  is related to the liquid-water path  $\mathcal{L}$  and cloud-droplet effective radius  $r_e$  through (Han *et al.*, 1994)

$$\tau_c = \frac{9 \mathcal{L}}{5 r_e}. \quad (3)$$

The liquid-water path  $\mathcal{L}$ , in turn, depends on the cloud geometric thickness  $h$  and degree of adiabaticity  $f_{\text{ad}}$ , given approximately by (Feingold *et al.*, 2017; Wood, 2006)

$$\mathcal{L} \approx f_{\text{ad}} h^2. \quad (4)$$

LWCRE is primarily determined by the cloud-top temperature  $T_c$  and its emissivity  $\epsilon$ , following the Stefan–Boltzmann law, with

$$\text{LWCRE} \approx \epsilon \sigma T_c^4, \quad (5)$$

where  $\sigma$  represents the Stefan–Boltzmann constant (Ardanuy *et al.*, 1991). Since  $T_c$  can be approximated by cloud-top height  $z_t$ , deeper clouds tend to be colder, emitting less LW radiation to space, thereby resulting in more LW radiative warming. Since our focus is on shallow clouds, the LWCRE variability is minimal and SWCRE variability will govern the net CRE variability; we show this in Section 3.1. In the following sections, we will therefore use the relations above to interpret how remotely sensed and simulated  $f_c$ ,  $\tau_c$ ,  $\mathcal{L}$ ,  $r_e$ ,  $f_{\text{ad}}$ , and  $h$  make up variations in SWCRE, due only to the spatial patterning of clouds.

Following previous studies (Bony *et al.*, 2020; Janssens *et al.*, 2021; Stevens *et al.*, 2020), we focus on clouds over the tropical Atlantic Ocean to the east of Barbados ( $10^\circ$ – $20^\circ$ N,  $48^\circ$ – $58^\circ$ W), which have been shown to be representative for the trades (Medeiros & Nuijens, 2016). Our analysis covers December–May of 2002–2020. The satellite dataset used here combines data from NASA’s Moderate Resolution Imaging Spectroradiometer (MODIS) aboard the *Aqua* satellite, with data from the Clouds and the Earth’s Radiant Energy System (CERES) instrument. We compute organization metrics from MODIS cloud masks with 1-km spatial resolution. For each cloudy scene, we calculate two metrics: cloud fraction ( $f_c$ ) and degree of organization ( $I_{\text{org}}$ ). The metric  $I_{\text{org}}$  is derived based on the distribution of the nearest-neighbor distances (Janssens *et al.*, 2021; Weger *et al.*, 1992), which characterizes cloud fields as clustered when  $I_{\text{org}} > 0.5$ , random at  $I_{\text{org}} = 0.5$ , and regular for  $I_{\text{org}} < 0.5$ . The preprocessing of MODIS cloud masks follows Janssens *et al.* (2021): scenes with  $> 20\%$  cirrus coverage ( $\approx 5\%$  of the total data) are excluded, as are cloud fields with solar zenith angles  $> 45^\circ$  ( $\approx 15\%$  of the total data). In line with the analysis of Bony *et al.* (2020, fig. 5), we use the full  $10^\circ \times 10^\circ$  domain, which leads to excluding about 50% of the total data due to the

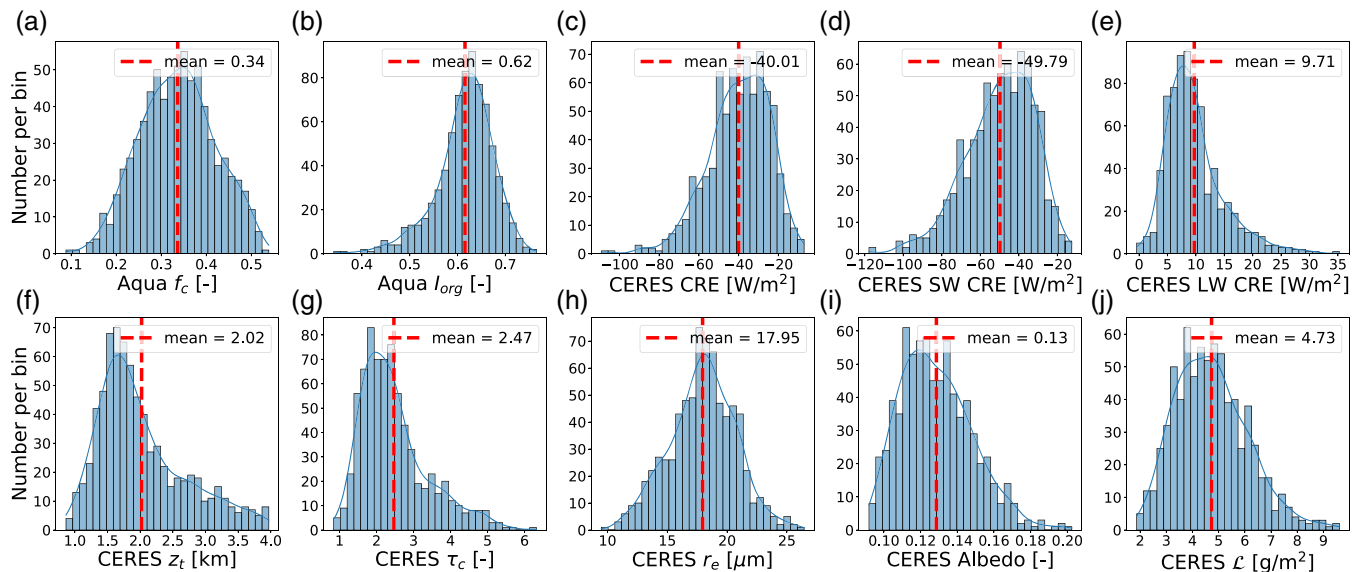


**FIGURE 1** Distribution of cloud field properties from *Aqua* MODIS and CERES satellite data. (a) Cloud fraction  $f_c$ , (b) degree of organization  $I_{org}$ , (c) domain-mean net cloud radiative effect (CRE), (d) domain-mean SWCRE, (e) domain-mean LWCRE, (f) domain-mean cloud-top height  $z_t$ , (g) domain-mean cloud optical depth  $\tau_c$ , (h) domain-mean cloud effective radius  $r_e$ , (i) domain-mean cloud field albedo, and (j) domain-mean liquid-water path  $\mathcal{L}$ . [Colour figure can be viewed at [wileyonlinelibrary.com](https://onlinelibrary.wiley.com)]

satellite swath not covering the whole  $10^\circ \times 10^\circ$  domain. Following Schulz *et al.* (2021), we focus solely on shallow clouds by excluding scenes with cloud-top heights  $z_t > 4$  km, which excludes about 5% of the total data. After preprocessing, out of about 3200 cloud scenes, approximately 750 cloud fields remain for analysis, which is about 25% of the total data. Nevertheless, the distributions of  $f_c$  and  $I_{org}$  shown in Figure 1a,b confirm that the remaining data still cover a rich spectrum of patterns, and are similar to distributions shown by Bony *et al.* (2020).

CERES provides hourly top-of-the-atmosphere SW and LW radiative fluxes for all-sky and clear-sky conditions, as well as  $\tau_c$ ,  $A_c$ ,  $z_t$ ,  $\mathcal{L}$ , and  $r_e$ . The CERES dataset features a spatial resolution of  $1^\circ$ . We select CERES data around 13:30 local time, which corresponds to the overpass time of the *Aqua* satellite. SWCRE and LWCRE are calculated as the difference between the all-sky and clear-sky radiative fluxes at the top of the atmosphere. For each cloud scene, we calculate domain-mean values of cloud properties provided by CERES. The distributions of CERES data are shown in Figure 1c–j.

We extend our satellite analysis with the *Cloud Botany* dataset (Jansson *et al.*, 2023). This is a large ensemble (ca. 100 members) of high-resolution (100-m) large-eddy simulations (LES) of shallow cumulus clouds with a domain size of 150 km by 150 km. It was initialized with a variety of conditions derived from ERA5 reanalysis data (Hersbach *et al.*, 2020) of trade cumuli that cover the climatological conditions of the area under consideration.

We refer to the dataset article, Jansson *et al.* (2023), for details. Our motivation for employing the *Botany* simulations is twofold. Firstly, considering that satellite retrievals of liquid-water path  $\mathcal{L}$  (and effective radius  $r_e$ ) might be underestimated (overestimated) in broken cloud fields containing small clouds (Cho *et al.*, 2015; Coakley *et al.*, 2005; Painemal & Zuidema, 2011; Seethala & Horváth, 2010; Zhang & Platnick, 2011), the simulations support that our results are physical. Secondly, the simulations provide data on cloud-base height ( $z_b$ ) and cloud geometric thickness ( $h$ ), so that we can investigate how those vertical characteristics are correlated to organization. The distributions of lifting condensation level as well as  $z_b$  (Figure S1) show qualitative agreement with those of Barbados Cloud Observatory data as shown in Albright *et al.* (2023, figs. 2, 3). We use hourly data from hours 37–43 of the simulations (574 cloud fields in total). These times are chosen because they approximately align with the daily overpass times of the *Aqua* satellite to match the diurnal phase. To determine the geometric thickness  $h$  of each cloudy column, we calculate the difference between the altitudes of the highest and lowest cloudy pixels where the liquid water specific humidity is larger than zero. Subsequently, for each cloud field, we compute the domain-averaged  $h$ . We further compute the mean size of cloud objects within each cloud field using  $L_c = (\sum_1^n \sqrt{A_i})/n$ , where  $A_i$  represents the area of each individual cloud object  $i$ , and  $n$  corresponds to the total number of cloud objects within the field.

### 3 | RESULTS AND DISCUSSION

#### 3.1 | Cloud clustering impacts CRE independently of $f_c$ variability

Bony *et al.* (2020) showed that trade cumulus mesoscale organization affects CRE through variations in  $f_c$ : scenes with organization types of higher cloud cover have a larger, negative CRE. In this section, we aim to investigate whether mesoscale organization still affects CRE,

independently of  $f_c$ . Figure 2a–c shows that more clustered clouds (higher  $I_{org}$ ) reflect less SW radiation towards space (smaller magnitude of SWCRE). In addition, increased clustering is also correlated with decreased LWCRE. Overall, the warming effect induced by the SW component is partially compensated by the reduced LW warming. Consequently, enhanced clustering of clouds results in diminished net cloud radiative cooling.

It is crucial to emphasize that the relationships illustrated in Figure 2a–c are confounded by the variability of

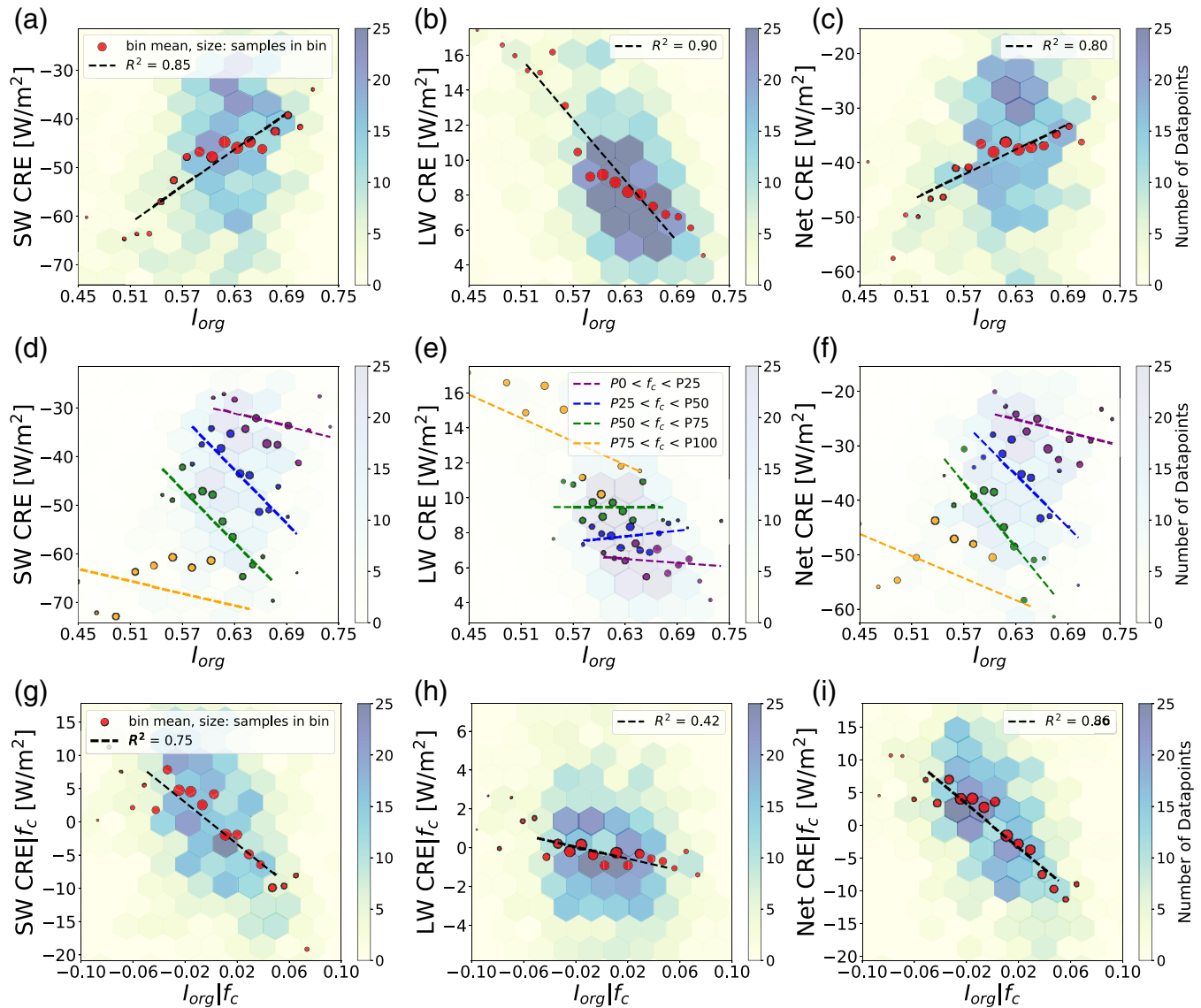


**FIGURE 2** Dependence of domain-mean CRE on clustering. In the first row (a–c), the relationships between  $I_{org}$  and (a) SWCRE, (b) LWCRE, and (c) net CRE are illustrated. The second row (d–f) presents the same relationships, but the data are grouped into four classes based on the 0th (P0), 25th (P25), 50th (P50), 75th (P75), and 100th (P100) percentiles of  $f_c$ , indicated by colors ranging from purple to yellow, representing low to high  $f_c$ , respectively. The third row (g–i) shows the same relationships, but removing the  $f_c$  variability through partial correlation analysis (Equation 6). The mean values of  $I_{org}$  (for the third row,  $I_{org}/f_c$ ) in each bin are denoted by red (purple, blue, green, and yellow for the third row) circles, with their size proportional to the number of points in the bin. The dots are fitted with a dashed line. Values below the 5th and above the 95th percentile of  $I_{org}$  (for the third row,  $I_{org}/f_c$ ) are excluded from the fit. [Colour figure can be viewed at [wileyonlinelibrary.com](http://wileyonlinelibrary.com)]



$f_c$ , as  $f_c$  is correlated with  $I_{\text{org}}$  ( $R^2 = 0.61$ ), SWCRE ( $R^2 = 0.51$ ), and LWCRE ( $R^2 = 0.34$ ) (see also Figures S2, 2d,e). To understand better how  $f_c$  controls the relationships between organization and radiation, Figure 2d–f presents the same data as Figure 2a–c, but grouped into quartiles of  $f_c$ . Figure 2d shows that, although  $I_{\text{org}}$  and SWCRE exhibit a positive correlation across the entire dataset (Figure 2a), they demonstrate a negative correlation within each  $f_c$  bin. Hence, the relationship between  $I_{\text{org}}$  and SWCRE presented in Figure 2a emerges because  $I_{\text{org}}$  itself depends on  $f_c$  (purple to yellow lines in Figure 2d–f). Once we remove this correlation between  $I_{\text{org}}$  and  $f_c$ , for example, by binning on  $f_c$ , we observe that the SWCRE becomes more negative when the cloud fields become more clustered (lines at constant  $f_c$  have a negative slope). Similarly, Figure 2e shows that the strong negative  $I_{\text{org}}$ –LWCRE correlation (Figure 2b) is almost entirely due to variations in  $f_c$ ; it almost vanishes upon grouping the data by  $f_c$ . The net CRE is dominated by its SW component (Figure 2f), and therefore follows the results from Figure 2d. Hence, Figure 2a–c essentially captures the findings by Bony *et al.* (2020), showing that, to first order, variations in  $f_c$  control variations in SWCRE.

To eliminate the confounding effect of  $f_c$  on the  $I_{\text{org}}$ –CRE relationship, we employ the concept of partial correlation analysis (Baba *et al.*, 2004). For any given metric (e.g.,  $X$ ), we eliminate the variability associated with  $f_c$  using a regression analysis,

$$X = c \cdot f_c + X|f_c, \quad (6)$$

where  $f_c$  serves as the regressor,  $c$  represents the coefficient, and  $X|f_c$  denotes the remaining variability in  $X$  that cannot be explained by  $f_c$ . It should be noted that Equation (6) does not keep  $f_c$  constant. In a scatter plot with a linear fit  $c \cdot f_c$ ,  $X|f_c$  instead measures the distance from the regression line (Figure S3). Partial correlation is conceptually similar to grouping data by a confounding variable, as in Figure 2d–f, but it controls continuously for the confounder across the whole dataset. This gives more statistically significant correlations compared with simple grouping, where the number of data points can decrease drastically after the grouping has been performed. The different colors in Figure 2d–f correspond to subtracting different offsets  $c \cdot f_c$  from  $X$ . By measuring the distance from the central fit line, the method thus collapses all the lines in Figure 2d–f into a single line.

Figures 2g–i present the variables with their partial correlation to  $f_c$  removed. Figure 2g shows that, as  $I_{\text{org}}|f_c$  increases, SWCRE $|f_c$  becomes more negative, that is, as clouds cluster, they reflect more incoming SW radiation. Quantitatively, as  $I_{\text{org}}|f_c$  varies between  $-0.05$  and  $0.05$ , the radiative cooling induced by SW reflection

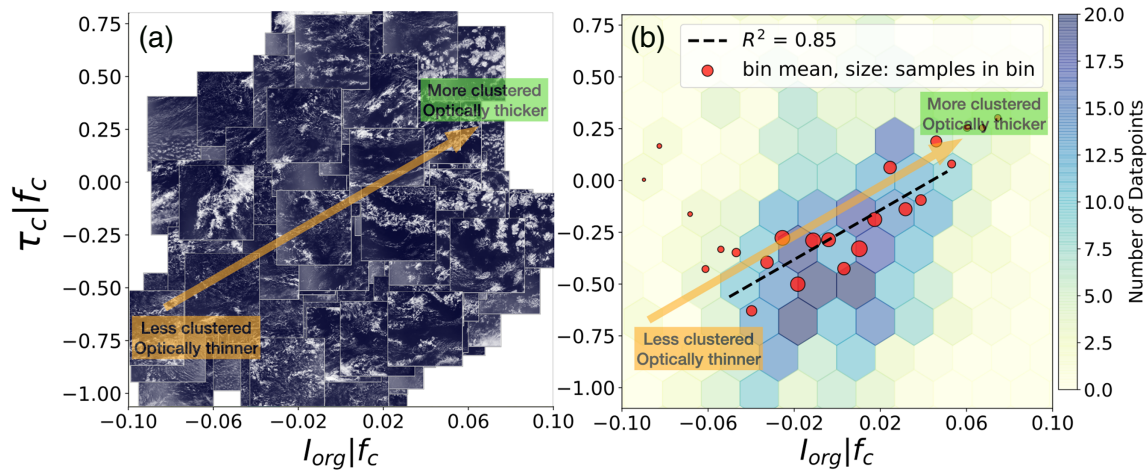
increases by approximately  $20 \text{ W/m}^2$ . This confirms that the positive correlation observed in Figure 2a is due to  $I_{\text{org}}$  and SWCRE being negatively correlated with  $f_c$  (Figure 2d). Similarly, after elimination of  $f_c$  variability, the response of LWCRE to cloud clustering is strongly reduced to about  $1 \text{ W/m}^2$  (Figure 2h), indicating that the correlation between  $I_{\text{org}}$  and LWCRE in Figure 2b is almost solely due to their mutual correlation with  $f_c$  (Figure 2e). The variability in LWCRE due to clustering is thus similar in magnitude to the LW radiative effect ( $\approx 0.75 \text{ W/m}^2$ ) of the “cloud twilight zone” (Eytan *et al.*, 2020). Ultimately, as Figure 2i illustrates, the dependence of net CRE on  $I_{\text{org}}|f_c$  arises almost exclusively from the dependence of the SW component on cloud clustering. In summary, our findings of this section emphasize that mesoscale organization affects CRE, even after controlling for  $f_c$  variability.

### 3.2 | Clustering and cloud optical thickness are positively correlated

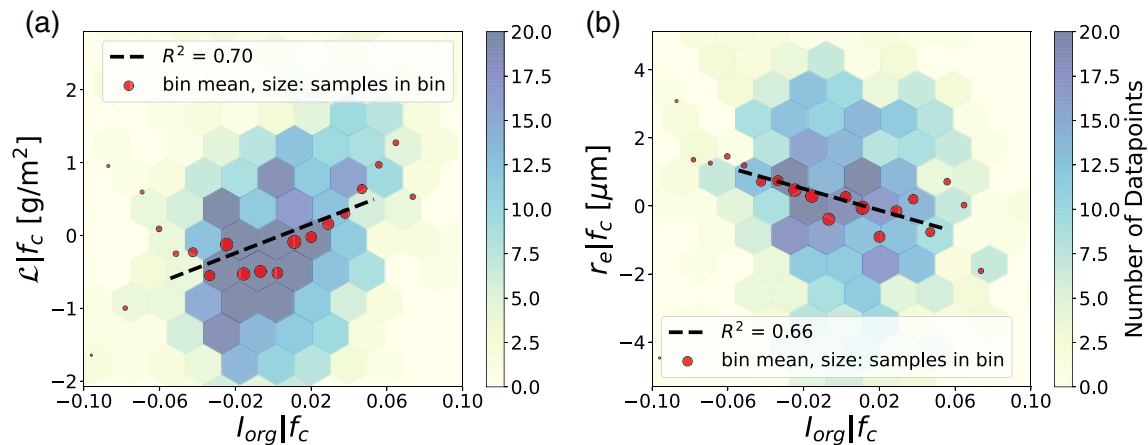
In the previous section, we eliminated the impact of  $f_c$  on the  $I_{\text{org}}$ –SWCRE relationship. The remaining variability in SWCRE after controlling for  $f_c$  is primarily due to variations in  $A_c$  (Equation 1): a bilinear regression with  $f_c$  and  $A_c$  as regressors can explain 94% of variability in SWCRE in our dataset (Figure S4). This confirms that the impact of 3D radiative effects is small compared with  $f_c$  and  $A_c$  in these large cloud fields. Having 3D effects excluded, the remaining variability in SWCRE corresponds primarily to changes in cloud albedo and equivalently cloud optical depth  $\tau_c$  (Equation 2).

Figure 3a displays the variability of cloud patterns in a plane spanned by  $\tau_c|f_c$  and  $I_{\text{org}}|f_c$ . This figure shows a continuous range of patterns, ranging from small, unclustered clouds in the lower left corner to large, highly clustered clouds in the upper right corner. On average,  $\tau_c|f_c$  increases with increasing  $I_{\text{org}}|f_c$  (Figure 3b). Quantitatively, a 0.1 increase in  $I_{\text{org}}|f_c$  corresponds to a 0.5 increase in  $\tau_c|f_c$ , which is about 10% of the total  $\tau_c$  variability (Figure 1g). Such a 0.1 increase in  $I_{\text{org}}|f_c$  results in an approximately 0.01 increase in the domain-mean albedo (Figure S5). In trade-wind regimes, even such small albedo variability makes up a non-negligible portion (roughly 10%, Figure 1i) of the total albedo variability, consistent with Denby (2023). The relationship between  $I_{\text{org}}|f_c$  and  $\tau_c|f_c$  indicates that horizontal cloud field organization, as measured by  $I_{\text{org}}$ , is linked to its optical properties, as captured by  $\tau_c$ : trade cumuli are optically thicker when they are more clustered.

As theoretically expected (Equation 3),  $\tau_c$  is proportional to  $\mathcal{L}/r_c$  in our dataset (Figure S6). Figure 4



**FIGURE 3** Dependence of domain-mean cloud optical depth on clustering. (a) The scatter plot of MODIS cloud features and (b) the two-dimensional histogram depict the  $I_{\text{org}}|f_c - \tau_c|f_c$  relationship. Specifically, for the scatter plot in (a), instead of displaying individual points, the entire cloud field is visualized to enhance pattern visualization. Clouds are represented in white, while the blue background represents the ocean color (MODIS true-color images). For plot (b), the mean values of  $I_{\text{org}}|f_c$  in each bin are denoted by red circles, with their size proportional to the number of points in the bin. The red dots are fitted with a dashed black line. Values below the 5th and above the 95th percentile of  $I_{\text{org}}|f_c$  are excluded from the fit. [Colour figure can be viewed at wileyonlinelibrary.com]



**FIGURE 4** Dependence of domain-mean liquid water path and effective radius on clustering. The figure shows the 2D histograms of the relationships between (a)  $I_{\text{org}}|f_c$  and  $\mathcal{L}|f_c$ , and (b)  $I_{\text{org}}|f_c$  and  $r_e|f_c$ . The mean values of  $I_{\text{org}}|f_c$  in each bin are denoted by red circles, with their size proportional to the number of points in the bin. The red dots are fitted with a dashed black line. Values below the 5th and above the 95th percentile of  $I_{\text{org}}|f_c$  are excluded from the fit. [Colour figure can be viewed at wileyonlinelibrary.com]

shows that both  $\mathcal{L}$  and  $r_e$  contribute to mediating the relationship between clustering and optical depth. With the  $f_c$  effect eliminated, there is a positive correlation between the degree of cloud clustering and the amount of liquid water present within the clouds (Figure 4a). Similarly, as the level of clustering increases, clouds tend to exhibit smaller radii  $r_e$  (Figure 4b).

Stevens *et al.* (2020) introduced a subjective classification of patterns, which they termed *Sugar*, *Gravel* and *Flowers*. *Sugar* consists of small randomly distributed clouds. *Gravel* is associated with ring-like structures. Their organization is not as random as for the *Sugar* type but

still features values of  $I_{\text{org}}$  that indicate an unclustered state. *Flowers* are commonly highly clustered groups of circular clouds with clear-sky regions between them. Our  $\mathcal{L}$ - $I_{\text{org}}$  relationship seems to be in contrast to Schulz *et al.* (2021), who show that individual clouds in unclustered *Gravel* configuration have higher liquid-water path  $\mathcal{L}$  compared with individual clouds in *Flowers* configuration, which is highly clustered. To reconcile this with our results, we need to remind ourselves that the large cloud scenes analyzed here contain a mixture of different clouds. Stevens *et al.* (2020) report that *Gravel* clouds tend to coexist with *Sugar*. For *Flowers*, such a coexistence is less

pronounced. Instead, *Flowers* feature anvils, stratiform outflows that form once the updrafts encounter stable layers such as the inversion, causing the cloud to grow horizontally. Such shallow cumulus anvils have notable geometric thickness (up to 600 m: Dauhut *et al.*, 2023). This means that anvil cloudiness is optically thicker and more reflective than typical *Sugar*. When considering two cloud fields with identical  $f_c$ , it therefore seems reasonable that a *Flower*-dominated field features a larger domain-averaged  $\mathcal{L}$  compared with a field dominated by *Sugar* and *Gravel*.

Similarly, the relationship between  $I_{\text{org}}$ ,  $\mathcal{L}$ , and  $r_e$  might seem unexpected. Based on adiabatic parcel lifting, we would expect  $\mathcal{L}$  and  $r_e$  to be positively correlated, while Figure 4 suggests a negative correlation. When correlating  $\mathcal{L}$  versus  $r_e$  directly, we find the expected positive correlation, as shown in Figure 5. However, Figure 5 shows further that, with increasing  $I_{\text{org}}|f_c$ ,  $\mathcal{L}$  increases while  $r_e$  decreases, indicating that more clustered cloud fields contain more liquid water with smaller effective radius. To hypothesize why, we use an example snapshot from a scene (Figure S7a) at the high end of the  $I_{\text{org}}|f_c$  values: in such scenes, clouds have substantially smaller  $r_e$  in their veils compared with their core updrafts. In contrast, unclustered cloud fields exhibit a more homogeneous  $r_e$  with relatively larger values (Figure S7b). These snapshots

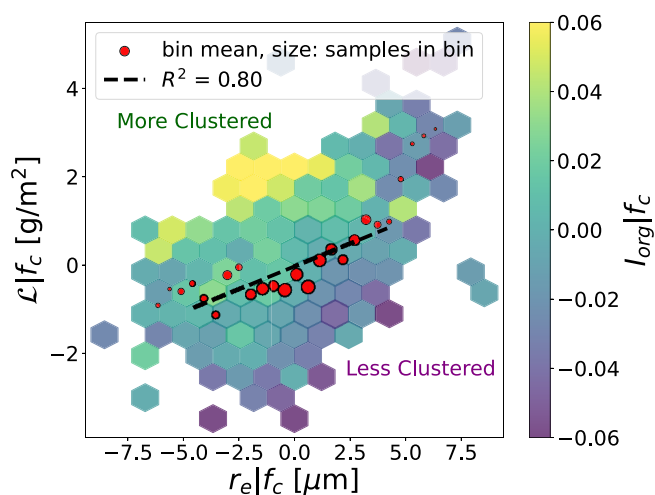


**FIGURE 5** Relationship between domain-mean liquid-water path and effective radius. This figure shows that  $\mathcal{L}|f_c$  is positively correlated with  $r_e|f_c$ . The figure further shows that with increased clustering  $I_{\text{org}}|f_c$ , that is, going from the lower right corner to the upper left corner,  $r_e$  decreases while  $\mathcal{L}$  increases. The mean values of  $r_e|f_c$  in each bin are denoted by red circles, with their size proportional to the number of points in the bin. The red dots are fitted with a dashed black line. Values below the 5th and above the 95th percentile of  $r_e|f_c$  are excluded from the fit. [Colour figure can be viewed at [wileyonlinelibrary.com](https://onlinelibrary.com)]

suggest that, for highly clustered cloud fields, the average  $\mathcal{L}$  is influenced primarily by their cores, while the average  $r_e$  is influenced by their veils. This is consistent with the fact that  $\mathcal{L}$  is proportional to  $r_e^6$  (Goren *et al.*, 2022), resulting in a more pronounced contrast between the core and veils in  $\mathcal{L}$  compared with  $r_e$ . This could well explain why the average  $\mathcal{L}$  of highly clustered cloud fields is larger compared with that of unclustered cloud fields, while their average  $r_e$  is smaller in comparison with unclustered cloud fields.

It is of utmost importance to recognize that satellite retrievals of  $\mathcal{L}$  and  $r_e$  over broken clouds come with uncertainties, as documented in previous studies (Painemal & Zuidema, 2011; Seethala & Horváth, 2010; Zhang & Platnick, 2011). These uncertainties can result in an overestimation of  $r_e$  and an underestimation of  $\mathcal{L}$ , especially for small clouds, such as *Sugar* and *Gravel*. This is because these clouds might feature smaller sizes compared with the resolution of satellites ( $\approx 1$  km), leading to more frequent partially filled pixels (Cho *et al.*, 2015; Coakley *et al.*, 2005). By utilizing standard satellite products, which exclude highly uncertain pixels associated with very small clouds (see Figure S7b), these biases are mitigated to some extent and enhance the reliability of our analysis of  $r_e$  and  $\mathcal{L}$ . Nonetheless, it is essential to note that this analysis urges the need for further modeling or in situ observational studies exploring the relationship between the organization and microphysics of trade cumulus clouds.

It is interesting to contrast the small droplets in relatively thick anvils described here with the very large droplet sizes and optically thin veil clouds that have been reported in the context of the stratocumulus-to-cumulus transition (Wood *et al.*, 2018). While Wood and Bretherton (2018) report an increase in the corresponding ultra-clean conditions with boundary-layer height, this relationship is unlikely to extend to deep trade cumulus *Flowers*, which can be considered shallow mesoscale convective systems with complex outflow dynamics (Dauhut *et al.*, 2023). On the microphysical process level, ultra-clean conditions have been associated with strong precipitation scavenging (Wood & Tseng, 2018), while Radtke *et al.* (2023) discuss that the conversion efficiency to precipitation decreases with increasing clustering in trade cumulus.

Overall, our discussion of the relationship between liquid-water path and effective radius to clustering and the resulting effects on optical depth highlight that organized cloud fields cannot be conceptualized with a single, typical profile of cloudiness. Instead, addressing horizontal spatial variability necessitates the consideration of at least two distinct cloud types, associated with horizontal variations in the profiles of liquid water and droplet sizes (see sketches in Figure 7 later).



### 3.3 | Mean cloud geometric thickness increases with clustering

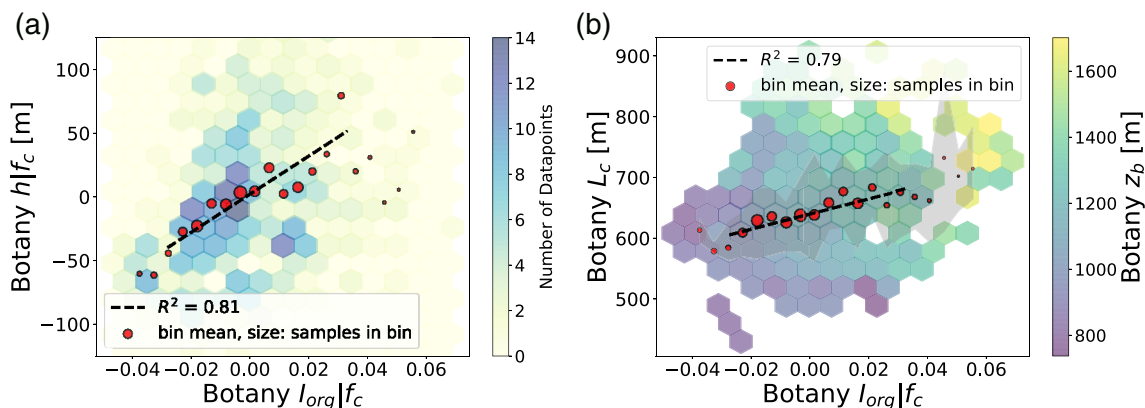
For an entraining lifting parcel, liquid-water path  $\mathcal{L} \propto f_{\text{ad}} h^2$  (Equation 4). To explain the observed  $I_{\text{org}}-\mathcal{L}$  relationship, we therefore investigate the relationships of  $I_{\text{org}}$  with geometric cloud depth  $h$  and degree of adiabaticity  $f_{\text{ad}}$  in the *Botany* simulations. We repeat the analysis from Sections 3.1 and 3.2 for the *Botany* dataset. We notice that the correlation between  $f_c$  and  $I_{\text{org}}$  is smaller ( $R$  of 0.1) in the *Botany* dataset that features smaller domain size compared with our satellite data (Figure S8a). This is in line with the results of Janssens *et al.* (2021) on satellite data over 500-km domains in which the  $f_c-I_{\text{org}}$  correlation ( $R$ ) is about 0.3 (their fig. S2 in the supplementary information). This shows that the  $f_c-I_{\text{org}}$  correlation decreases on reducing the domain size. We hypothesize that reducing the domain size increases the variability in  $f_c$ , with  $f_c$  potentially reaching values of 1 (Figure S9). Conversely, reducing the domain size decreases the probability of a cloud field featuring more than one type of pattern, thus reducing the variability in  $I_{\text{org}}$  (Figure S9). Therefore, with increased  $f_c$  towards 1,  $I_{\text{org}}$  cannot decrease to less than a limit, as reduced domain size shrinks its variability. This potentially decreases the covariance between  $f_c$  and  $I_{\text{org}}$ , weakening the strength of the  $f_c-I_{\text{org}}$  correlation.  $f_c$  and  $I_{\text{org}}$  being almost orthogonal in the *Botany* data (Figure S8a) implies that combinations of  $f_c$  and  $I_{\text{org}}$  explain most patterns that develop in the *Botany* dataset, and their relation to  $\tau$  and the CRE might be understood without controlling for  $f_c$  (Janssens, 2023, chap. 7). Here, we still remove the effect of  $f_c$  from both CRE and  $I_{\text{org}}$ , to investigate solely the effect of  $I_{\text{org}}$  on CRE independent

of  $f_c$  variations and remain consistent with the analysis in Section 3.1.

Repeating the analysis for the simulation data shows qualitative agreement with the observations (Figures S10a–c and S11) and thus justifies using the simulations to analyze the relationships between  $I_{\text{org}}$ ,  $h$ , and  $f_{\text{ad}}$  further. Note that the discrepancy in the response of  $r_e$  to clustering between simulations and satellite data (Figure S10d) is expected from the fixed cloud droplet number in the simulations, but does not fundamentally affect our discussion of  $\mathcal{L}$  here.

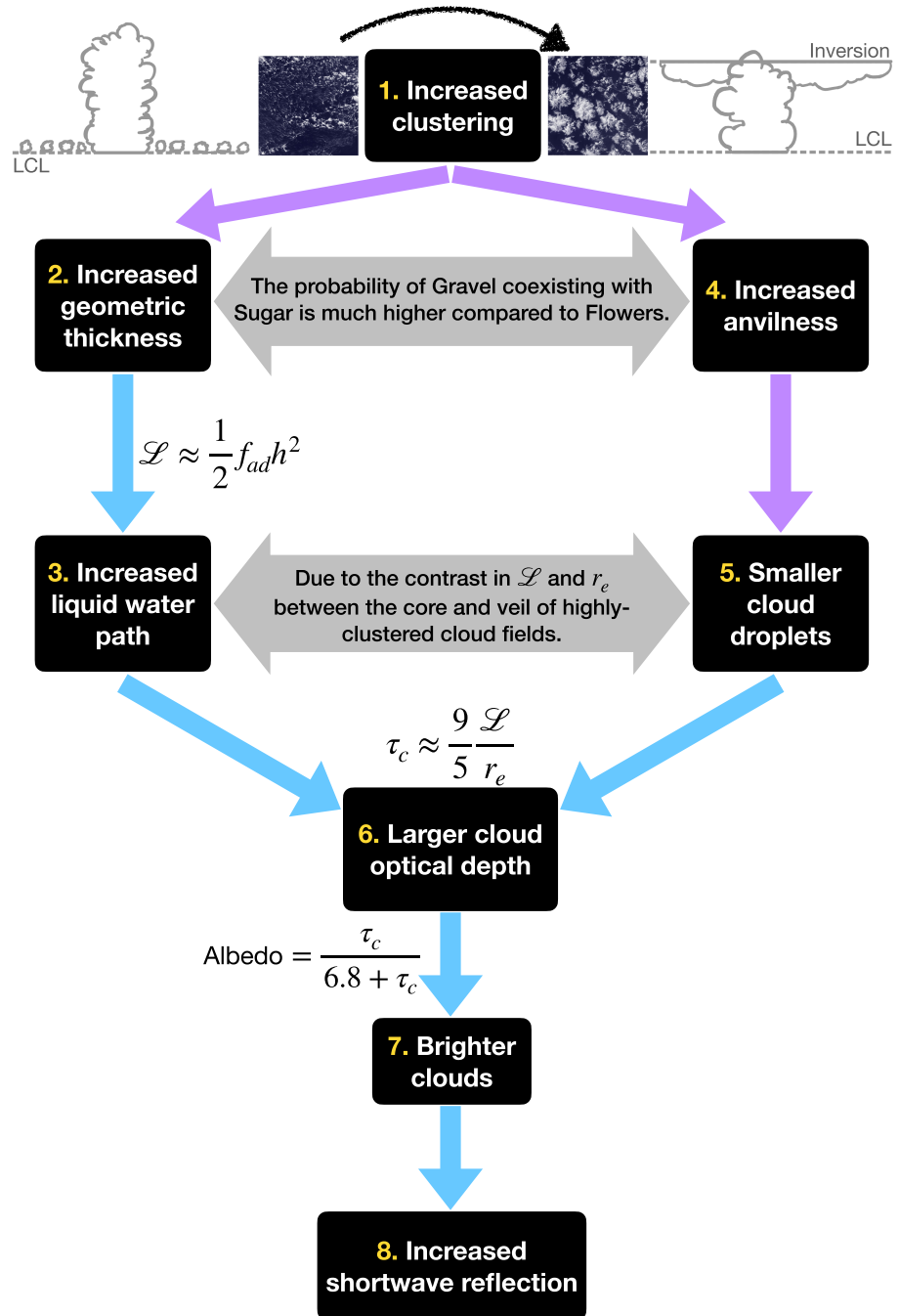
Figure 6a shows that the domain-averaged geometric thickness increases by more than 100 m as cloud fields become more clustered (increasing  $I_{\text{org}}|f_c$ ). Additionally, compared with  $f_{\text{ad}}$ , the variability in  $h$  has a significantly larger influence on the value of  $\mathcal{L}$  (Figure S12). Thus, our LES-based results indicate that the simulated increase in  $\mathcal{L}$  due to enhanced clustering (Figure S10c) stems primarily from the geometric thickening of cloud fields.

Figure 6b further explores the relationship between horizontal and vertical cloud field properties and shows that the average size of cloud objects ( $L_c$ ) increases with  $I_{\text{org}}|f_c$ . This positive correlation shows that cloud horizontal extent as quantified by  $L_c$  is positively correlated with cloud vertical extent as quantified by  $h$ , consistent with the findings of Feingold *et al.* (2017). The figure moreover illustrates that an increase in  $I_{\text{org}}|f_c$  corresponds to a rise in the domain-average cloud-base height ( $z_b$ ). Note that  $z_b$  is not the lifting condensation level; instead, it represents the lowest height of a cloudy pixel within each column. This means that a higher domain-mean  $z_b$  is an indication of the presence of more anvils in the field. Overall, Figure 6 demonstrates that enhanced clustering



**FIGURE 6** Dependence of domain-mean geometric thickness, average size of cloud objects, and domain-mean cloud-base height on clustering. (a) The figure shows the 2D histogram of the relationship between  $I_{\text{org}}|f_c$  and  $h|f_c$ . (b) The plot shows the relationship between  $I_{\text{org}}|f_c$  and the mean-field cloud object size ( $L_c$ ), with contour colors representing the values of domain-averaged cloud-base height ( $z_b$ ). The gray shade indicates the inter-quartile range variability of  $L_c$  in each bin of  $I_{\text{org}}|f_c$ . For both plots, the mean values of  $I_{\text{org}}|f_c$  in each bin are denoted by red circles, with their size proportional to the number of points in the bin. The red dots are fitted with a dashed black line. For both plots, values below the 5th and above the 95th percentile of  $I_{\text{org}}|f_c$  are excluded from the fit. [Colour figure can be viewed at [wileyonlinelibrary.com](http://wileyonlinelibrary.com)]

**FIGURE 7** Summary of results. Comparing two cloud fields with identical cloud cover, the highly clustered cloud field features a larger domain-averaged geometric thickness, a higher liquid water path, more frequent anvils with smaller cloud droplets, and, consequently, brighter clouds and therefore larger SW reflection in comparison with the unclustered cloud field. Blue arrows and corresponding equations are supported by theory and thus imply causality. Purple arrows are the main results of our study, which only indicate correlations. The gray arrows illustrate apparent paradoxes, which are discussed in Section 3.2. [Colour figure can be viewed at [wileyonlinelibrary.com](http://wileyonlinelibrary.com)]



is correlated with a higher occurrence of larger cloud objects with elevated domain-mean  $z_b$ , indicating a larger anvil extent.

## 4 | CONCLUSIONS AND OUTLOOK

We have explored the impact of shallow cumulus cloud field organization on cloud radiative effects, where confounding variability of  $f_c$  was removed through partial correlation analysis (Equation 6). Based on satellite data, our analysis shows that an increased level of clustering

( $I_{\text{org}}|f_c$ ) results in up to  $20 \text{ W/m}^2$  higher SW reflection to space (Figure 2g,i). We observe that, irrespective of  $f_c$  variations, more clustered cloud fields exhibit, on average, higher liquid water path (Figure 4a), smaller cloud droplets (Figure 4b), and, consequently, greater optical thickness (Figure 3). A complementing ensemble of large-eddy simulations indicates that increased clustering corresponds to geometrically thicker cloud fields that feature increased anvilliness (Figure 6). Figure 7 summarizes these results. Collectively, they suggest that, eliminating the effect of  $f_c$ , the distribution of horizontal cloud sizes ultimately relates to the vertical

extent of clouds, subsequently influencing liquid-water path and cloud optical depth, and ultimately albedo and SWCRE.

What do our results mean in terms of the cloud feedback of trade cumulus? To translate the potential impact of increased SW radiative cooling from organization (independently of  $f_c$ ) into cloud feedback estimates, a worthwhile follow-up effort would be to repeat our analysis for all trade-wind regions. Such global statistics would contribute to a comprehensive quantification of the sensitivity of CRE to  $I_{\text{org}}$ . Considering the sensitivity of mesoscale organization to cloud-controlling factors, Myers *et al.* (2021) (their Supplementary Information) show that, in addition to an increase in sea-surface temperature, which is not expected to trigger a notable response in trade cumulus cloudiness (Cesana & Del Genio, 2021; Myers *et al.*, 2021), estimated inversion strength (EIS) is projected to increase moderately, and surface wind to decrease slightly. According to Bony *et al.* (2020), such an increase in EIS would favor high-cloud-fraction *Flowers* over *Gravel* and *Sugar* with lower cloud fractions. In contrast, the decreasing surface wind would favor *Sugar*. While our results highlight the tight relationship between horizontal cloud organization and geometric thickness, whether cloud fraction and optical depth interact positively or negatively in response to drivers of organization remains an open question. To address this interplay, we need to explore further how mesoscale processes (George *et al.*, 2023; Janssens *et al.*, 2023; Vogel *et al.*, 2021) modulate cloud fraction, liquid-water path, effective radii, and anvil extent.

## ACKNOWLEDGEMENTS

For the *Botany* dataset, this work used resources of the Deutsches Klimarechenzentrum (DKRZ) granted by its Scientific Steering Committee (WLA) under project ID bm1349. In the final stages of preparing this article, we became aware of independent, related, and to-date still unpublished work by Denby (2023). We thank Guy Dagan and one anonymous reviewer for their insightful feedback. F. Glassmeier and P. Alinaghi acknowledge support from The Branco Weiss Fellowship—Society in Science, administered by ETH Zurich. F. Glassmeier also acknowledges a NWO Veni grant. A. Pier Siebesma acknowledges support from the European Union's Horizon 2020 research and innovation program under grant agreement no. 820829 (CONSTRAIN project). T. Goren acknowledges funding by the German Research Foundation (Deutsche Forschungsgemeinschaft, DFG; GZ QU 311/27-1) for project "CDNC4ACI." G. Choudhury acknowledges startup funds from Bar-Ilan University.

## CONFLICT OF INTEREST STATEMENT

The authors have no conflict of interest.

## DATA AVAILABILITY STATEMENT

The cloud masks, provided by *Aqua* satellites, related to NASA's MODIS instrument, can be extracted from the level-1 Atmosphere Archive & Distribution System Distributed Active Archive Center ([http://dx.doi.org/10.5067/MODIS/MYD06\\_L2.061](http://dx.doi.org/10.5067/MODIS/MYD06_L2.061)). The dataset related to the CERES instrument is made available by Synoptic TOA and surface fluxes and clouds (SYN1deg-level 3) at <https://ceres.larc.nasa.gov/data/#syn1deg-level-3>. Prepossessing of cloud masks alongside calculation of organization metrics were done using the cloud metrics Github repository available at <https://github.com/cloudsci/cloudmetrics>. The Botany dataset was downloaded using the EUREC<sup>4</sup>A intake catalog ([https://howto.eurec4a.eu/botany\\_daies.html](https://howto.eurec4a.eu/botany_daies.html)). The data were analyzed utilizing Python (used libraries: Numpy (Harris *et al.*, 2020), Pandas (McKinney, 2010), Scipy (Virtanen *et al.*, 2020), Matplotlib (Hunter, 2007), and Seaborn (Waskom, 2021)). ChatGPT (OpenAI: <https://openai.com/blog/chatgpt>) has been used for copy-editing during the preparation of the article. The data availability statement is provided in the article.

## ORCID

Pouriya Alinaghi  <https://orcid.org/0000-0003-4536-0205>

## REFERENCES

- Albright, A.L., Stevens, B., Bony, S. & Vogel, R. (2023) A new conceptual picture of the trade wind transition layer. *Journal of the Atmospheric Sciences*, 80, 1547–1563.
- Ardanuy, P.E., Stowe, L.L., Gruber, A. & Weiss, M. (1991) Shortwave, longwave, and net cloud-radiative forcing as determined from nimbus 7 observations. *Journal of Geophysical Research: Atmospheres*, 96, 18537–18549.
- Baba, K., Shibata, R. & Sibuya, M. (2004) Partial correlation and conditional correlation as measures of conditional independence. *Australian & New Zealand Journal of Statistics*, 46, 657–664.
- Bony, S. & Dufresne, J.-L. (2005) Marine boundary layer clouds at the heart of tropical cloud feedback uncertainties in climate models. *Geophysical Research Letters*, 32, L20806.
- Bony, S., Dufresne, J.-L., Le Treut, H., Morcrette, J.-J. & Senior, C. (2004) On dynamic and thermodynamic components of cloud changes. *Climate Dynamics*, 22, 71–86.
- Bony, S., Schulz, H., Vial, J. & Stevens, B. (2020) Sugar, gravel, fish, and flowers: dependence of mesoscale patterns of trade-wind clouds on environmental conditions. *Geophysical Research Letters*, 47, e2019GL085988.
- Bony, S., Stevens, B., Frierson, D.M., Jakob, C., Kageyama, M., Pinus, R. *et al.* (2015) Clouds, circulation and climate sensitivity. *Nature Geoscience*, 8, 261–268.
- Cesana, G.V. & Del Genio, A.D. (2021) Observational constraint on cloud feedbacks suggests moderate climate sensitivity. *Nature Climate Change*, 11, 213–218.

- Cho, H.-M., Zhang, Z., Meyer, K., Lebsock, M., Platnick, S., Ackerman, A.S. et al. (2015) Frequency and causes of failed modis cloud property retrievals for liquid phase clouds over global oceans. *Journal of Geophysical Research: Atmospheres*, 120, 4132–4154.
- Coakley, J.A., Friedman, M.A. & Tahnk, W.R. (2005) Retrieval of cloud properties for partly cloudy imager pixels. *Journal of Atmospheric and Oceanic Technology*, 22, 3–17.
- Dauhut, T., Couvreur, F., Bouniol, D., Beucher, F., Volkmer, L., Pörtge, V. et al. (2023) Flower trade-wind clouds are shallow mesoscale convective systems. *Quarterly Journal of the Royal Meteorological Society*, 149, 325–347.
- Denby, L. (2020) Discovering the importance of mesoscale cloud organization through unsupervised classification. *Geophysical Research Letters*, 47, e2019GL085190.
- Denby, L. (2023) Charting the realms of mesoscale cloud organisation using unsupervised learning. <https://doi.org/10.48550/arXiv.2309.08567>
- Eytan, E., Koren, I., Altaratz, O., Kostinski, A.B. & Ronen, A. (2020) Longwave radiative effect of the cloud twilight zone. *Nature Geoscience*, 13, 669–673.
- Feingold, G., Balsells, J., Glassmeier, F., Yamaguchi, T., Kazil, J. & McComiskey, A. (2017) Analysis of albedo versus cloud fraction relationships in liquid water clouds using heuristic models and large eddy simulation. *Journal of Geophysical Research: Atmospheres*, 122, 7086–7102.
- George, G., Stevens, B., Bony, S., Vogel, R. & Naumann, A.K. (2023) Widespread shallow mesoscale circulations observed in the trades. *Nature Geoscience*, 16, 584–589.
- Goren, T., Feingold, G., Gryspeerd, E., Kazil, J., Kretzschmar, J., Jia, H. et al. (2022) Projecting stratocumulus transitions on the albedo—cloud fraction relationship reveals linearity of albedo to droplet concentrations. *Geophysical Research Letters*, 49, e2022GL101169.
- Han, Q., Rossow, W.B. & Lacis, A.A. (1994) Near-global survey of effective droplet radii in liquid water clouds using isccp data. *Journal of Climate*, 7, 465–497.
- Harris, C.R., Millman, K.J., van der Walt, S.J., Gommers, R., Virtanen, P., Cournapeau, D. et al. (2020) Array programming with NumPy. *Nature*, 585, 357–362. Available from: <https://doi.org/10.1038/s41586-020-2649-2>
- Hersbach, H., Bell, B., Berrisford, P., Hirahara, S., Horányi, A., Muñoz-Sabater, J. et al. (2020) The ERA5 global reanalysis. *Quarterly Journal of the Royal Meteorological Society*, 146, 1999–2049.
- Hunter, J.D. (2007) Matplotlib: a 2D graphics environment. *Computing in Science & Engineering*, 9, 90–95.
- Janssens, M. (2023) *Mesoscale Cloud Patterns in the Trade-Wind Boundary Layer*. Ph.D. thesis. Wageningen: Wageningen University. p. 288. Available from: <https://doi.org/10.18174/635857>
- Janssens, M., de Arellano, J.V.-G., van Heerwaarden, C.C., de Roode, S.R., Siebesma, A.P. & Glassmeier, F. (2023) Nonprecipitating shallow cumulus convection is intrinsically unstable to length scale growth. *Journal of the Atmospheric Sciences*, 80, 849–870.
- Janssens, M., Vilà-Guerau de Arellano, J., Scheffer, M., Antonissen, C., Siebesma, A.P. & Glassmeier, F. (2021) Cloud patterns in the trades have four interpretable dimensions. *Geophysical Research Letters*, 48, e2020GL091001.
- Jansson, F., Janssens, M., Grönqvist, J.H., Siebesma, A.P., Glassmeier, F., Attema, J. et al. (2023) Cloud botany: shallow cumulus clouds in an ensemble of idealized large-domain large-eddy simulations of the trades. *Journal of Advances in Modeling Earth Systems*, 15, e2023MS003796.
- Johnson, R.H., Rickenbach, T.M., Rutledge, S.A., Ciesielski, P.E. & Schubert, W.H. (1999) Trimodal characteristics of tropical convection. *Journal of Climate*, 12, 2397–2418.
- Lacis, A.A. & Hansen, J. (1974) A parameterization for the absorption of solar radiation in the earth's atmosphere. *Journal of Atmospheric Sciences*, 31, 118–133.
- Luebke, A.E., Ehrlich, A., Schäfer, M., Wolf, K. & Wendisch, M. (2022) An assessment of macrophysical and microphysical cloud properties driving radiative forcing of shallow trade-wind clouds. *Atmospheric Chemistry and Physics*, 22, 2727–2744.
- McCoy, I.L., McCoy, D.T., Wood, R., Zuidema, P. & Bender, F.A.-M. (2022) The role of mesoscale cloud morphology in the shortwave cloud feedback. *Geophysical Research Letters*, 50, e2022GL101042.
- McKinney, W. (2010) Data structures for statistical computing in python. In: van der Walt, S. & Millman, J. (Eds.) *Proceedings of the 9th python in science conference*, pp. 56–61. Available from: <https://doi.org/10.25080/Majora-92bf1922-00a>.
- Medeiros, B. & Nuijens, L. (2016) Clouds at Barbados are representative of clouds across the trade wind regions in observations and climate models. *Proceedings of the National Academy of Sciences*, 113, E3062–E3070.
- Myers, T.A., Scott, R.C., Zelinka, M.D., Klein, S.A., Norris, J.R. & Caldwell, P.M. (2021) Observational constraints on low cloud feedback reduce uncertainty of climate sensitivity. *Nature Climate Change*, 11, 501–507.
- Nuijens, L. & Siebesma, A.P. (2019) Boundary layer clouds and convection over subtropical oceans in our current and in a warmer climate. *Current Climate Change Reports*, 5, 80–94.
- Painemal, D. & Zuidema, P. (2011) Assessment of MODIS cloud effective radius and optical thickness retrievals over the southeast pacific with VOCALS-REX in situ measurements. *Journal of Geophysical Research: Atmospheres*, 116, D24206.
- Radtke, J., Vogel, R., Ament, F. & Naumann, A.K. (2023) Spatial organisation affects the pathway to precipitation in simulated trade-wind convection. *Geophysical Research Letters*, 50, e2023GL103579.
- Ramanathan, V., Cess, R., Harrison, E., Minnis, P., Barkstrom, B., Ahmad, E. et al. (1989) Cloud-radiative forcing and climate: results from the earth radiation budget experiment. *Science*, 243, 57–63.
- Schneider, T., Teixeira, J., Bretherton, C.S., Brient, F., Pressel, K.G., Schär, C. et al. (2017) Climate goals and computing the future of clouds. *Nature Climate Change*, 7, 3–5.
- Schulz, H., Eastman, R. & Stevens, B. (2021) Characterization and evolution of organized shallow convection in the trades. *Journal of Geophysical Research: Atmospheres*, 126, e2021JD034575.
- Seethala, C. & Horváth, Á. (2010) Global assessment of AMSR-E and MODIS cloud liquid water path retrievals in warm oceanic clouds. *Journal of Geophysical Research: Atmospheres*, 115, D13202.
- Singer, C.E., Lopez-Gomez, I., Zhang, X. & Schneider, T. (2021) Top-of-atmosphere albedo bias from neglecting three-dimensional cloud radiative effects. *Journal of the Atmospheric Sciences*, 78, 4053–4069.
- Stevens, B., Bony, S., Brogniez, H., Hentgen, L., Hohenegger, C., Kiemle, C. et al. (2020) Sugar, gravel, fish and flowers: mesoscale



- cloud patterns in the trade winds. *Quarterly Journal of the Royal Meteorological Society*, 146, 141–152.
- Tobin, I., Bony, S. & Roca, R. (2012) Observational evidence for relationships between the degree of aggregation of deep convection, water vapor, surface fluxes, and radiation. *Journal of Climate*, 25, 6885–6904.
- Tompkins, A.M. & Semie, A.G. (2017) Organization of tropical convection in low vertical wind shears: role of updraft entrainment. *Journal of Advances in Modeling Earth Systems*, 9, 1046–1068.
- Virtanen, P., Gommers, R., Oliphant, T.E., Haberland, M., Reddy, T., Cournapeau, D. et al. (2020) SciPy 1.0: fundamental algorithms for scientific computing in python. *Nature Methods*, 17, 261–272.
- Vogel, R., Albright, A.L., Vial, J., George, G., Stevens, B. & Bony, S. (2022) Strong cloud–circulation coupling explains weak trade cumulus feedback. *Nature*, 612, 696–700.
- Vogel, R., Konow, H., Schulz, H. & Zuidema, P. (2021) A climatology of trade-wind cumulus cold pools and their link to mesoscale cloud organization. *Atmospheric Chemistry and Physics*, 21, 16609–16630.
- Waskom, M.L. (2021) Seaborn: statistical data visualization. *Journal of Open Source Software*, 6, 3021. Available from: <https://doi.org/10.21105/joss.03021>
- Weger, R., Lee, J., Zhu, T. & Welch, R. (1992) Clustering, randomness and regularity in cloud fields: 1. Theoretical considerations. *Journal of Geophysical Research: Atmospheres*, 97, 20519–20536.
- Wood, O.K.-T. & Bretherton, C.S. (2018) Ultraclean layers and optically thin clouds in the stratocumulus-to-cumulus transition. Part II: depletion of cloud droplets and cloud condensation nuclei through collision–coalescence. *Journal of the Atmospheric Sciences*, 75, 1653–1673.
- Wood, O.K.-T. & Tseng, H. (2018) Deeper, precipitating PBLs associated with optically thin veil clouds in the Sc-Cu transition. *Geophysical Research Letters*, 45, 5177–5184.
- Wood, R. (2006) *Relationships between optical depth, liquid water path, droplet concentration, and effective radius in adiabatic layer cloud*. Washington: University of Washington, p. 3. Available from: [https://atmos.uw.edu/~robwood/papers/chilean\\_plume/optical\\_depth\\_relations.pdf](https://atmos.uw.edu/~robwood/papers/chilean_plume/optical_depth_relations.pdf)
- Wood, R., Bretherton, O.K.-T., Mohrmann, C.S., Albrecht, J., Zuidema, B.A., Ghate, P. et al. (2018) Ultraclean layers and optically thin clouds in the stratocumulus-to-cumulus transition. Part I: observations. *Journal of the Atmospheric Sciences*, 75, 1631–1652.
- Zhang, Z. & Platnick, S. (2011) An assessment of differences between cloud effective particle radius retrievals for marine water clouds from three MODIS spectral bands. *Journal of Geophysical Research: Atmospheres*, 116, D20215.

## SUPPORTING INFORMATION

Additional supporting information can be found online in the Supporting Information section at the end of this article.

**How to cite this article:** Alinaghi, P., Janssens, M., Choudhury, G., Goren, T., Siebesma, A.P. & Glassmeier, F. (2024) Shallow cumulus cloud fields are optically thicker when they are more clustered. *Quarterly Journal of the Royal Meteorological Society*, 1–12. Available from: <https://doi.org/10.1002/qj.4783>